CrossMark

J. Plasma Phys. (2020), *vol*. 86, 905860517 © The Author(s), 2020.
Published by Cambridge University Press
doi:10.1017/S0022377820001099

First experiments on ICRF discharge generation by a W7-X-like antenna in the Uragan-2M stellarator

V. E. Moiseenko [1],†, Yu. V. Kovtun [1], T. Wauters [2], A. Goriaev[2], A. I. Lyssoivan[2], A. V. Lozin [1], R. O. Pavlichenko[1], A. N. Shapoval[1], S. M. Maznichenko[1], V. B. Korovin[1], E. D. Kramskoy[1], M. M. Kozulya [1], N. V. Zamanov[1], Y. V. Siusko [1], A. Yu. Krasiuk [1], V. S. Romanov[1], A. Alonso [3], R. Brakel[4], A. Dinklage[4], D. Hartmann [4], Ye. Kazakov[2], H. Laqua[4], J. Ongena[2], T. Stange[4] and the Uragan-2M Team

[1]Institute of Plasma Physics of the National Science Center "Kharkiv Institute of Physics and Technology", Kharkiv, Ukraine

[2]Laboratory for Plasma Physics, ERM/KMS, Brussels, Belgium

[3]Laboratorio Nacional de Fusion, CIEMAT, Madrid, Spain

[4]Max-Planck-Institut für Plasmaphysik, Greifswald, Germany

(Received 17 May 2020; revised 24 August 2020; accepted 1 September 2020)

In support of the ICRF experiments planned on the Wendelstein 7-X (W7-X) stellarator, i.e. fast ion generation, wall conditioning, target plasma production and heating, a first experimental study on plasma production has been made in the Uragan-2M (U-2M) stellarator using W7-X-like two-strap antenna. In all the experiments, antenna monopole phasing was used. The W7-X-like antenna operation with launched radiofrequency power of ∼100 kW have been performed in helium ($p = (4–14) \times 10^{-2}$ Pa) with the vacuum vessel walls pre-loaded with hydrogen. Production of plasma with a density higher than 10^{12} cm^{-3} was observed near the first harmonic of the hydrogen cyclotron frequency. Operation at first hydrogen harmonic is feasible in W7-X future ICRF experiments.

Key words: fusion plasma, plasma heating, plasma devices

1. Introduction

The world biggest stellarator Wendelstein 7-X (W7-X) will resume operation in the next few years (Klinger *et al.* 2019; Pedersen *et al.* 2019). The ion-cyclotron plasma heating (ICRH) system (Ongena *et al.* 2014) will be installed at it among other new equipment.

The microwave heating at the second electron-cyclotron resonance (ECR) harmonics is the main scenario for plasma production and heating at the W7-X device (Wolf *et al.* 2019). The magnetic field range for operation is mostly limited around the vicinity of 2.5 T value because the ECR zone should be present inside the plasma column. There is an option to use heating at third ECR harmonics in the 1.7 T magnetic field

† Email address for correspondence: moiseenk@kipt.kharkov.ua

https://doi.org/10.1017/S0022377820001099 Published online by Cambridge University Press

(Erckmann *et al.* 2007; Marushchenko *et al.* 2019). Experiments at this magnetic field are of certain interest. First, they will give a possibility to determine the influence of the magnetic field on plasma confinement, plasma instabilities, equilibrium electric currents, etc. Second, because W7-X mechanical stresses are reduced in this case, it will be possible to study more magnetic configurations. In addition, studying the physics of the electron-cyclotron heating at third harmonics is of interest. The magnetohydrodynamic (MHD) stability studies (Nührenberg 2016) and high-beta equilibrium investigations (Geiger *et al.* 2015) need more magnetic configuration space of W7-X than is available at 2.5 T.

The first problem of operation at the lower magnetic field (1.7 T) is plasma production. Although plasma production is reliable at the second ECR harmonic, it is not observed at the third harmonic. An alternative possibility is plasma production using neutral beam injection (NBI), which is available at W7-X. The calculations (Gradic *et al.* 2015) show a delay of about 5 s between NBI start and full ionization of the neutral gas. This means that during that time almost all beam energy would be delivered to the armour installed at the opposite of the injector wall. The time of 5 s is excessively long and such a plasma production regime would result in unacceptably high thermal load on the armour (Äkäslompolo *et al.* 2019; van Eeten *et al.* 2019).

The radiofrequency (RF) discharge becomes an attractive opportunity in such a situation. Calculations in the paper by Gradic et al. (2015) indicate that successful plasma production with the NBI for less than 0.5 s needs a target plasma with a density of 10^{10}–10^{11} cm^{-3}. Other plasma parameters such as temperature and ion composition are not very important. Thus, the production of such a plasma is a minimum task for the RF discharge. After successful plasma production, the NBI can increase plasma density and temperature (approximately to 500 eV) until the microwave beam can be effectively absorbed at the third harmonic of ECR (Marushchenko *et al.* 2019).

Note that the RF heating equipment of W7-X has a wide frequency range, 25–38 MHz (Ongena *et al.* 2014), which provides the ion-cyclotron resonance (ICR) for hydrogen ions inside the plasma column at 2.5 and 1.7 T magnetic field. The RF heating equipment also gives a possibility of inner vacuum surfaces conditioning in hydrogen or other chemically active gas atmosphere with an RF discharge.

For plasma production, a scenario was developed and used on Uragan devices with frame antennae (Lyssoivan *et al.* 1992) and frequencies below the ion cyclotron. This scenario does not fit well with W-7X because its ICRH antenna is of a different type and consists of two vertically oriented straps. The antennae with vertical straps are used at tokamaks for plasma production for wall conditioning purposes (see, e.g., Li *et al.* 2011). In those discharges, the plasma density was below 1×10^{12} cm^{-3} without full ionization of the neutral gas. A bit higher plasma density and temperature was achieved in at W7-AS (Brakel *et al.* 2001) in a sophisticated two-step two-frequency scenario. Uragan-3M and Uragan-2M (U-2M) have the THT antennae (Lozin *et al.* 2013; Moiseenko *et al.* 2019) with the π–0–π phased vertical straps. The experiments on plasma production with these antennae shown that they can produce plasma at a lower magnetic field than the frame antenna when the frequency is equal to the ion cyclotron frequency. This plasma production scenario is characterized by a long gas breakdown time during which there is almost no antenna loading, and low temperature of plasma produced. Thus, for vertical strap antennae, there is a need for a more efficient scenario of plasma production that in addition to plasma production gives the opportunity for successive plasma heating in the same pulse.

As the main gas for the experiments at U-2M, helium is chosen because it is one of the working gases at W7-X (Klinger *et al.* 2019). It is used in glow and ECR discharges for

https://doi.org/10.1017/S0022377820001099 Published online by Cambridge University Press

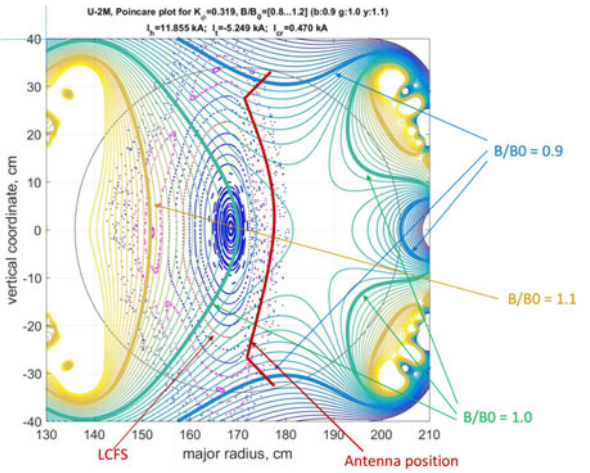


FIGURE 1. Poincaré plot of magnetic configuration and contours of magnetic field module at U-2M in antenna location. The circular line shows the vacuum chamber wall.

W7-X inner vacuum surface conditioning (Wauters *et al.* 2018). Helium ICR discharge was used earlier for vacuum chamber conditioning at W7-AS (Brakel *et al.* 2001), Tore Supra (Gauthier *et al.* 1997), TEXTOR-94 (Esser *et al.* 1997), HT-7 (HU *et al.* 2007) and EAST (HU *et al.* 2008).

The goal is to research helium plasma production in the U-2M stellarator device in the ion-cyclotron frequency range and to collect the information needed for W7-X plasma production scenario development.

The U-2M experimental setup is chosen to be mostly close to W7-X. Note here that both U-2M and W7-X are stellarators with topologically similar plasma column. The plasma confinement time is longer than the plasma start-up time in both machines. The gas types and pressure ranges are similar. The plasma density is lower at U-2M but still valuable for W-7X. For the experiments, a new W7-X-like antenna is installed at U-2M that has a $k_{\|}$ spectrum of similar shape. The magnetic field module behaviour at the antenna place is important for the plasma start-up scenario chosen. The magnetic field module contours at the antenna location at U-2M are shown in figure 1. They are not very topologically different from the contours at W7-X (Ongena *et al.* 2014).

The present paper gives the experimental results on plasma production at U-2M with a W-7X-like antenna. Section 2 describes the device, the W-7X-like antenna, the diagnostics and the experimental conditions. Section 3 discusses the experimental results of plasma production at the fundamental ion-cyclotron harmonic of hydrogen and gives some theoretical explanation to the experimental data. Section 4 summarizes the obtained results.

2. Description of the experiment

2.1. *Experimental setup*

The experiments on ICRF plasma build-up by the W7-X-like antenna were carried out in the U-2M stellarator-type device (see Pankratov *et al.* 2010; Moiseenko *et al.* 2011; Voitsenya *et al.* 2014; Moiseenko *et al.* 2016, 2017*a*). U-2M (see figure 2) was assembled in the early 1990s (Bykov *et al.* 1990; Pavlichenko 1993), operated briefly and then conserved. It was renewed and put to operation again at the end of 2006 (see Moiseenko *et al.* 2007; Beletskii *et al.* 2008).

https://doi.org/10.1017/S0022377820001099 Published online by Cambridge University Press

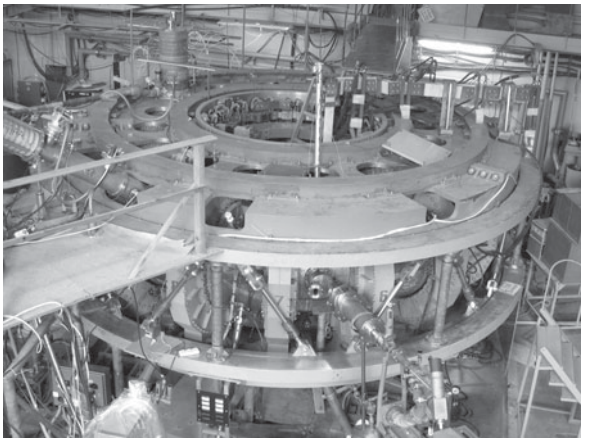


FIGURE 2. General view of Uragan-2M.

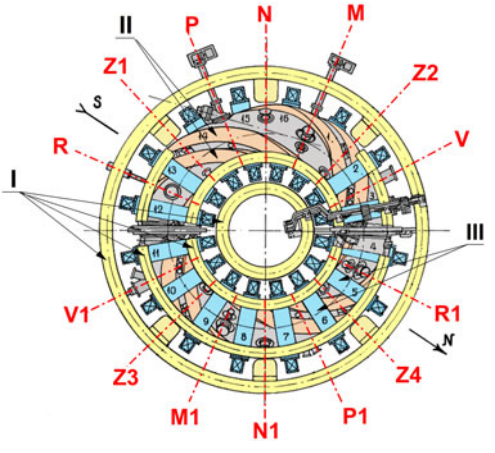


FIGURE 3. Scheme of Uragan-2M: I, poloidal field coils; II, helical field coils; III, toroidal field coils numbered 1–16. Different toroidal cross-sections are shown by red lines and denoted by capital letters and numbers.

The U-2M scheme is shown in figure 3. The major radius of the device is $R = 1.7$ m, the average plasma radius is $r_{pl} < 24$ cm and the toroidal magnetic field at the toroidal axis at present is $B_0 < 0.6$ T ($B_0 = B_{tt} + B_{th}$, B_{tt} and B_{th} are the toroidal fields produced by the toroidal and helical coils, respectively, the maximum magnetic field with respect to the mechanical stresses is $B_0 = 2.4$ T). The U-2M magnetic system consists of $l = 2$ helical coils with four periods ($m = 4$) in the toroidal direction. The minor radius of the helical coils is $r_h = 0.44$ m. The additional toroidal magnetic field is provided by a set of 16 circular toroidal coils evenly distributed along the torus. The poloidal coil system that consists of eight coils is mainly aimed at eliminating the vertical field induced by the helical coils. It includes four trim (correcting) coils for control of the residual vertical field and four coils for the magnetic island control. Two DC sources are used for power supply for the magnetic system. Each DC source consists of two generators P-22-33-17 K with a peak power of 2750 kW each. The generators are operated in a pulsed mode (see figure 4).

In the U-2M stellarator, the RF methods are used to produce and heat the plasma. For this purpose, two RF systems are used: ‘Kaskad-1’ (K-1) and ‘Kaskad-2’ (K-2) (Korovin

https://doi.org/10.1017/S0022377820001099 Published online by Cambridge University Press

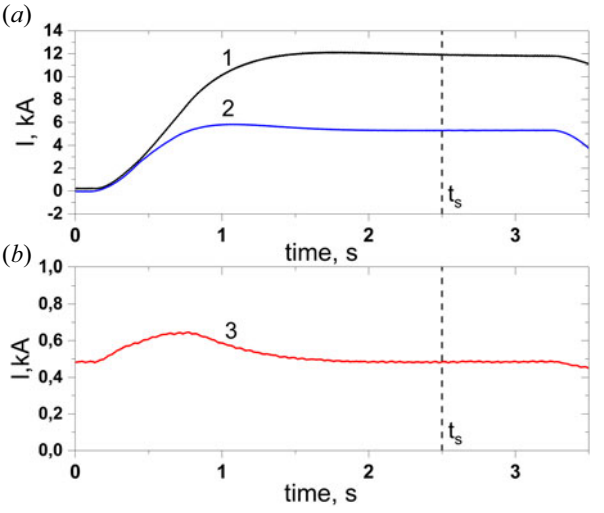


FIGURE 4. Time evolution of currents in helical (*a*, 1), toroidal (*a*, 2) and poloidal (correcting) (*b*, 3) coils of a magnetic system, where t_s is start time of the RF pulse.

& Kramskoy 2012). Both systems operate independently. Each RF system includes the RF generator, the transmission line, the matching circuit, the antenna and the control and diagnostic systems. The RF generators are single-staged and have a push–pull design. They use the GI-26A powerful tubes. Pairs of tubes are connected in parallel at each generator push–pull shoulder with the purpose of doubling the power output without increasing the anode voltage. The generators operate at a constant frequency in the range of 3–15 MHz and provide a pulse duration up to 100 ms. The maximum output power of the generators is about 0.8 MW. The output of the generators is coaxial bipolar. High-frequency power from the generator is delivered to the antenna by the feeder line, which consists of four coaxial cables (the RF cable RK-50-11-13 is used): two in each generator shoulder.

The toroidal vacuum chamber with the minor radius $r_c = 0.34$ m has a volume $V_c = 3.88\,\mathrm{m}^3$ (without vacuum ports) and the inner surface area of $S = 22.8\,\mathrm{m}^2$. There are 48 ports used for diagnostics, gas puffing, vacuum pumping, etc. The vacuum chamber is pumped by three turbo-molecular pumps TMN-500 (cross-sections V, Z1 and V1 in figure 2), each has a pumping speed of $0.5\,\mathrm{m}^3\,\mathrm{s}^{-1}$ and is equipped with a liquid nitrogen cryotrap aimed at trapping heavy gas molecules such as water and located between the pump and the vacuum chamber. Exhaust ends of the three turbo-molecular pumps are connected in parallel to the fore vacuum pump AVZ-63D (the pumping speed is $0.063\,\mathrm{m}^3\,\mathrm{s}^{-1}$) through the nitrogen cryotrap. The ultimate residual pressure in the vacuum chamber is 1.1×10^{-5} Pa. There is a mass spectrometer IPDO-2 of the omegatron type with the omegatron tube RMO-4S for measuring the residual gas partial pressures in the vacuum chamber. To measure the total pressure in the vacuum vessel, the thermocouple PMT-2 and the ionization PMI-2 and PMM-32-1 pressure gauges are used. The puffing of the working gas into the vacuum chamber is made using the SNA-2 stationary gas puff system.

2.2. *Two-strap antenna*

The U-2M has a history of ICRF plasma production and heating studies. The single and double frame, the crankshaft, the three-half-turn and the four-strap antennae (Pankratov *et al.* 2010; Moiseenko *et al.* 2011, 2016, 2017*a*) were used.

https://doi.org/10.1017/S0022377820001099 Published online by Cambridge University Press

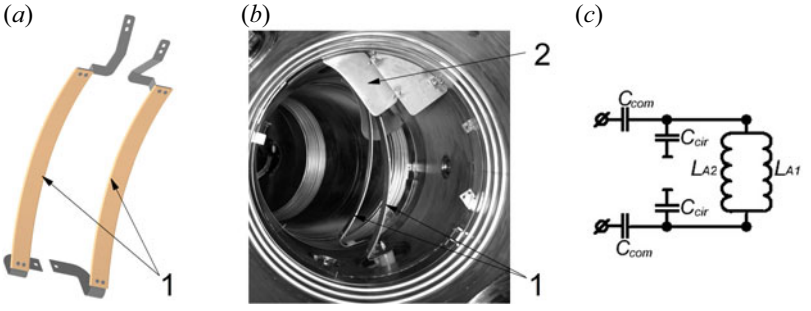


FIGURE 5. (*a*) Sketch of two-strap antenna, (*b*) two-strap antenna view in U-2M vacuum chamber (1 denotes straps, 2 denotes antenna limiter) and (*c*) connection scheme (L_{A1} and L_{A2} represent the antenna strap electric responses, C_{cir}, C_{com} are capacitors banks).

For plasma production studies, the existing vertical strap antenna, the THT antenna (Moiseenko *et al.* 2019), could be used. However, it does not excite low $k_{||}$ waves, and this could be an obstacle for plasma production (Lyssoivan *et al.* 2012, 2014).

Recently a new two-strap antenna was manufactured and installed at the U-2M stellarator. This antenna is similar in shape to the ICRH antenna of the W-7X and the main difference is that it is smaller. The antenna consists of two parallel poloidal straps (see figure 5*a*,*b*) made of stainless steel, 2 mm thick. The strap width is 60 mm and the length is 600 mm. The antenna is installed in the cross-section R1 (see figure 3). Its shape is fitted to the last closed flux surface, and the straps are placed at 10 mm distance from it (the magnetic configuration with $K_\varphi = 0.32$ is used, where $K_\varphi = B_{th}/(B_{tt} + B_{th})$). Two antenna straps are oriented perpendicular to the toroidal axis. Part of the plasma column comes too close to the antenna port, and at this place, the small limiters are inserted at both sides of the antenna. The main antenna elements and limiters are covered with titanium nitride film.

The two-strap antenna has four feeding points. The antenna can operate in different phasing, monopole or dipole, and be grounded or floating. This, in contrast to the THT antenna, gives more possibilities to control antenna $k_\parallel$ spectrum. The water cooling of the strap feed-throughs allows one to use the antenna in long pulses, up to 0.5 s. In the experiments reported here, the antenna operated in monopole phasing.

One of the electric connection schemes for monopole phasing is presented in figure 5(*c*). To match the impedance of the feeder line to the antenna, a matching device with a bi-polar L-circuit was used (Hayward 1994). For the dipole phasing, the serial connection of the straps is a possibility.

The RF power is calculated using the amplitudes of the forward and reflected waves in the feeder line measured by the directional coupler, according to the formula

$$P_{RF} = \frac{1}{2} \cdot \frac{|U_f|^2}{Z_0}(1 - |\Gamma|^2), \tag{2.1}$$

where Z_0 is the impedance of the transmission line, $Z_0 = 25\ \Omega$, $|\Gamma|$ is the reflection coefficient modulus, $|\Gamma| = |U_r|/|U_f|$, $|U_f|$ and $|U_r|$ are the voltage modules of the forward and reflected waves, respectively.

2.3. *Diagnostic methods*

As for plasma diagnostics, the time dependence of the linear electron density averaged over the line of sight was measured using a microwave interferometer (Pavlichenko, Zamanov &

https://doi.org/10.1017/S0022377820001099 Published online by Cambridge University Press

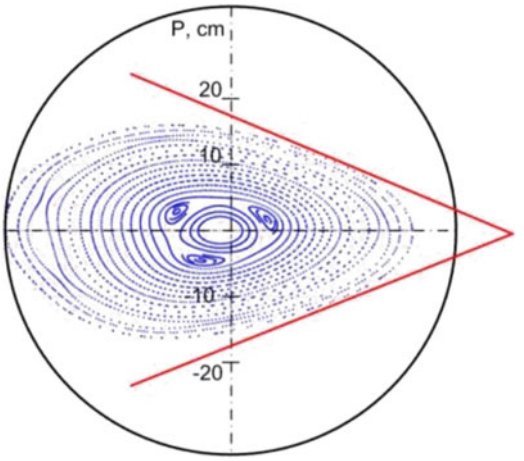


FIGURE 6. Sketch of chord measurements.

Kulaga 2017, 2018). The operational frequency of this super-heterodyne interferometer is equal to 140 GHz. The critical electron density for this frequency is 2.43×10^{14} cm^{-3}. The interferometer launches the ordinary polarized wave through the horizontal equatorial port along the minor axis of the elliptically shaped plasma in the cross-section R (see figure 3).

U-2M is equipped with the time-resolved optical emission spectroscopy (OES). OES was carried out using a monochromator-spectrograph SOLAR TII by SOL instruments Ltd, model MS7501i with Cherny–Turner optical scheme and a photomultiplier tube (PMT). The signals from the photomultiplier are amplified by a broadband amplifier and transmitted to the data acquisition system. The OES system has four independent channels. The database (Kramida *et al.* 2019) was used to identify the optical emission lines of atoms and ions. In addition to the integral emission registration, the scanning was made with 41 chords (see figure 6) in cross-section P1 (see figure 3). The chord distributions are measured using a pulse-by-pulse technique.

Signals from the microwave interferometer and OES system are transmitted via the fibreoptic transmission line to the data acquisition system. The data acquisition system of U-2M is based on the high-speed ADC modules L-CARD E-20-10 with maximum acquisition frequency 10 MHz and module L-CARD L-783 that is used only for the acquisition of the data from the RF directional coupler. The magnetic system, the RF system, the diagnostic equipment and the data acquisition system are synchronized with the U-2M timing facility (Lyashchenko *et al.* 2009).

3. Experimental results and discussion

3.1. *Discharge characteristics*

Helium was chosen as the working gas and hydrogen was always present during our experiments because the U-2M vacuum chamber inner surfaces were pre-loaded with hydrogen. Hydrogen ions are also produced by dissociative ionization of the residual water vapor and desorbed hydrogen-containing impurities from the wall.

The experiments were carried out at a helium pressure $p = 0.145$ Pa. The magnetic field value was $B_0 = 0.347$ T, $K_\varphi = 0.32$, the current in the poloidal correcting coil was $I_{corr} = 470$ A. The RF generator frequency was $f = 5.15$ MHz, whereas the hydrogen cyclotron frequency was 5.27 MHz at the axis of the torus. In this case $\omega \approx \omega_{ci}$ (H^+) $\approx 2\omega_{ci}$ (He^{2+}) $\approx 4\omega_{ci}$ (He^+). K-1 generator anode voltage was up to 7.5 kV. The timing was 10 ms

https://doi.org/10.1017/S0022377820001099 Published online by Cambridge University Press

(start), 11 ms (step 1, the first stepwise power increase), 12 ms (step 2, the final power increase) and 24 ms (shutdown). The RF generator anode voltage was varied stepwise as follows: $U_{a1} \approx 0.4 \cdot U_a$ at the start, $U_{a2} \approx 0.6 \cdot U_a$ at step 1 and maximal anode voltage U_a was set at step 2.

The RF power, the average density, and the spectral line intensities are shown in figure 7. Three stages could be separated in this discharge. The first stage is the plasma production that starts at 10 and ends at 15 ms. Figure 7 shows that the power radiated by the antenna varied significantly: P_{RF} is ~21 kW in the time interval between 10 ms (start) and 11 ms (step 1), P_{RF} is ~65 kW in the time interval between 11 ms (step 1) and 12 ms (step 2). The maximal power ~290 kW is registered after 12 ms (step 2) and later decreases down to ~160 kW. The initial plasma production and the plasma density growth occur at the first stage (the plasma production initial stage is discussed in detail in § 3.2). At the second stage that lasts from 15 to 18 ms, plasma density grows up to 2.4×10^{12} cm^{-3}. The atomic H* (H_Δ), He* (He I) spectral line intensities decrease and excited ions He^{+*} (He II), O^{+*} (O II) spectral line intensities increase until certain values. The power fed to the antenna is in the range of 160–190 kW.

The average plasma density changes in the range of $(2.2–2.6) \times 10^{12}$ cm^{-3} at the third stage that lasts from 18 to 24 ms while power fed to antenna decreases from 184 to 140 kW. Plasma decay begins after RF heating switch-off (24 ms). The average plasma density slowly ramps down with the characteristic time of about ~4 ms. He I, H_Δ and O II spectral lines intensities increase during the certain time after the RF heating switch-off, and He I afterglow is the most pronounced. It can be explained by electron temperature decrease and recombination of He^+, H^+ and O^{2+} ions with electrons. The absence of He II spectral line afterglow is likely a result of the small He^{2+} ion concentration in plasma. The ionization energy threshold for He^+ ion is 54.4 eV, for O^+ is 35.1 eV, for He is 24.6 eV and for H is 13.6 eV (Kramida *et al.* 2019). Thus, effective He^{2+} generation by electron impact ionization requires a higher temperature than O^{2+} generation. Note that the spectral lines of the ions O^{4+} (OV, the ionization energy threshold is 113.9 eV) and C^{4+} (CV, the ionization energy threshold is 392.1 eV) were not detected in the experiments. This means that the electron mean energy is much lower than the lowest previously cited threshold.

Figure 8 shows the dependency of the maximal average plasma density on the K-1 generator anode voltage. Plasma density does not exceed 1.2×10^{12} cm^{-3} at voltages lower than 6.5 kV, whereas it is about 2×10^{12} cm^{-3} at higher voltage. Further increase of the voltage does not result in increasing plasma density. Note that the average plasma density was of the same order as in other experiments for RF plasma production (see, e.g., Esser *et al.* 1997; Brakel *et al.* 2001).

3.2. *Start-up details*

Research on the initial plasma production stage of RF discharges in toroidal devices were carried out in experimental (Zaleskij *et al.* 1989; Carter *et al.* 1990; Lyssoivan *et al.* 2005; Moiseenko *et al.* 2017*b*, 2019) and theoretical (Lyssoivan *et al.* 1992, 2012; Moiseenko *et al.* 2013; Tripský *et al.* 2017; Wauters *et al.* 2020) studies. Following these studies, separate plasma production stages can be identified that are characterized by different physical pictures.

The first stage (non-wave stage) is the initial stage of plasma production. Here, the electromagnetic waves do not propagate in toroidal vacuum vessels of fusion devices because of the low charged particle density $\omega_{pe} < \omega$ (where ω_{pe} is the electron plasma frequency). The neutral gas is ionized by the electrons accelerated in the electric field of the RF antenna. The resulting low-density plasma ($N_e \ll N_0$, where N_0 is the density of

https://doi.org/10.1017/S0022377820001099 Published online by Cambridge University Press

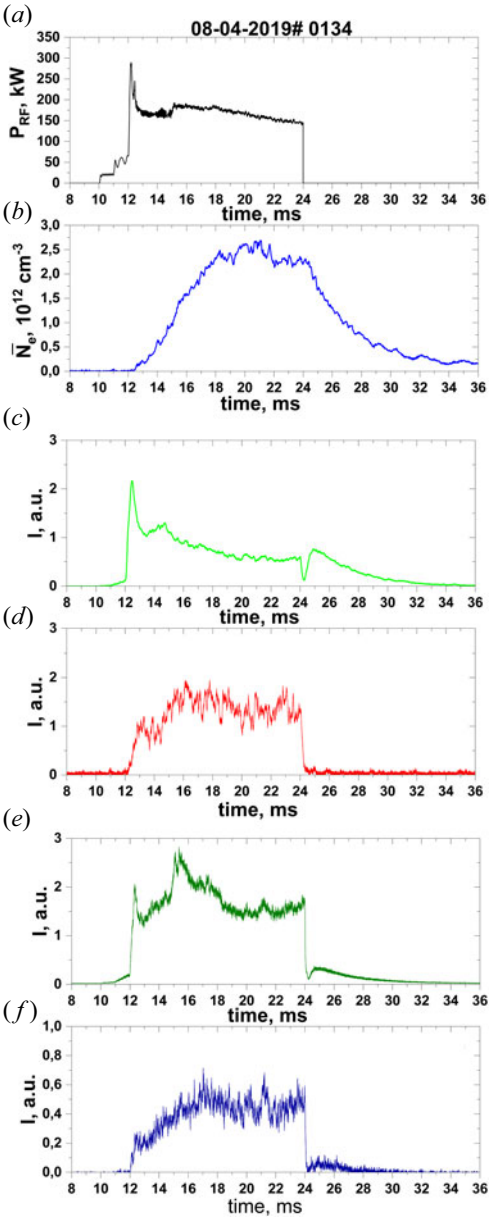


FIGURE 7. Time evolutions of (*a*) RF power and (*b*) average plasma density, and optical emission intensities of (*c*) He I, 447.15 nm, (*d*) He II, 468.6 nm, (*e*) H_{Δ}, 410.1 nm and (*f*) O II, 441.5 nm, where the K-1 generator anode voltage is $U_a = 7.5$ kV.

neutral particles) propagates along the magnetic field lines and practically has no influence on the electromagnetic field structure.

Numerical simulations show transition to a second stage when the wave propagation conditions are met $\omega_{pe} > \omega$ (Tripský *et al.* 2017), that cause an increase of the electron multiplication rate. Here, the plasma produced electrostatic field amplitude is of the same order as the vacuum $E_{||}$ field of the antenna. The plasma is mostly created via electron

https://doi.org/10.1017/S0022377820001099 Published online by Cambridge University Press

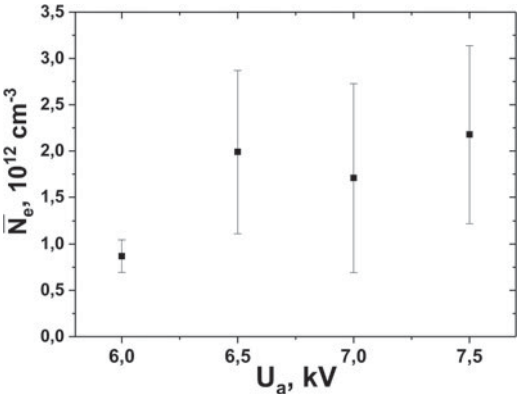


FIGURE 8. Maximum average plasma density as a function of the anode voltage on the generator K-1.

impact ionization. These collisions are accompanied by a significant electron power loss, which needs to be compensated for via the RF power supply.

At higher densities, the conditions given by the lower hybrid resonance $\omega^2 = \omega_{pi}^2 + \omega_{ci}^2$, the ICR $\omega = \omega_{ci}$ and the fast wave cut-off density $\omega_{pi}^2 = (N_\parallel^2 - 1)\omega_{ci}(\omega + \omega_{ci})$ determine the final radial extend of the discharge as well as the coupling efficiency of the RF power (Lyssoivan *et al.* 2012, 2014). Both electrons and ions are heated through collisional absorption of the electromagnetic waves, with the additional possibility for resonant absorption on ions in the case of ICR.

The time of plasma production can be associated with the time of appearance of excited atoms and ions in the plasma t_{app}. This is the time between RF pulse start-up and the start of the emission signal. Figure 9 shows t_{app} values for excited atoms and ions of helium, hydrogen and oxygen. As can be seen in figure 9, t_{app} is different for different optical lines and decreases with RF generator anode voltage increase. The optical emission by excited atoms have weaker dependence of $t_{app.}$ on U_a than that of the excited ions. The minimal values of t_{app} are observed for the hydrogen atom optical line H_Δ and helium line He I (figure 9*a*). H_Δ has a value of t_{app} between 0.13 and 0.2 ms, and the He I line has $t_{app} \approx 0.23$–0.35 ms accordingly. The t_{app} difference between H_Δ and He I line is likely a result of different energy thresholds and cross-section value of excitation by the electron impact. For H_Δ 410.1 nm and He I 447.15 nm lines, the corresponding thresholds are 13.2 and 23.7 eV accordingly (Kramida *et al.* 2019). Note that atomic hydrogen in ground or excited state appears in the discharge from electron impact with H_2 and other hydrogen-containing molecules in the processes of dissociation, dissociative ionization and dissociative attachment (Itikawa 2001).

In the experiments, H and He I optical line emissions appears at the RF generator step 1 (low-power operation) at time interval from 10 ms (start) to 11 ms (step 1). The RF plasma production start-up occurs in this time interval. Then the second (wave) discharge stage begins. The plasma density increases, and the excited ion lines appear, first oxygen and then helium (figure 9*b*). Here $t_{app} \approx 1.4$–2.3 ms for O II and $t_{app} \approx 1.9$–2.6 ms for He II. The times t_{app} cover different RF generator operational intervals. At low anode voltage, these lines appear at step 3 of K-1 operation. With increasing anode voltage, their start times migrate to step 2 (figure 9*b*). The difference of t_{app} for excited ions and atoms by an order of magnitude may be explained by a cascade mechanism of ion excitation (Kovtun, Shapoval & Siusko 2019). The corresponding thresholds for the lines O II 441.5 nm and

https://doi.org/10.1017/S0022377820001099 Published online by Cambridge University Press

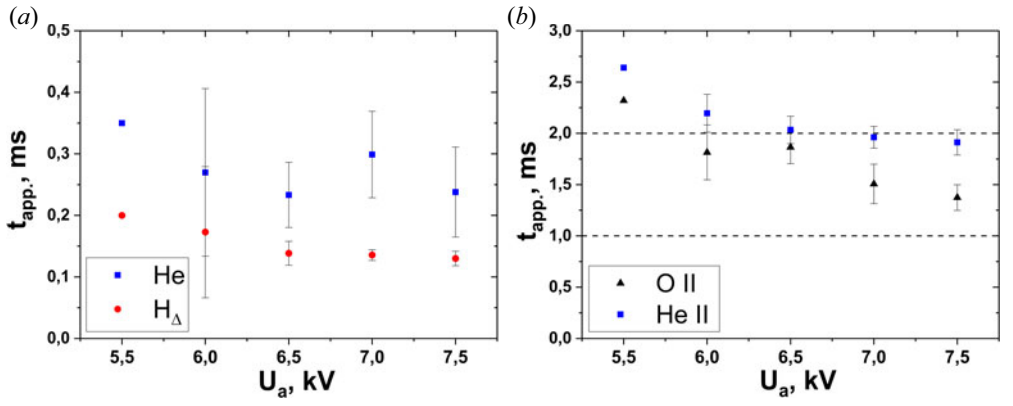


FIGURE 9. Time delay of spectral line emission appearing for (*a*) helium atoms He I 447.15 nm, H_Δ 410.1 nm and (*b*) ions He II 468.6 nm, O II 441.5 nm as a function of anode voltage of K-1 generator. Dashed lines show time moments of stepwise K-1 anode voltage increase.

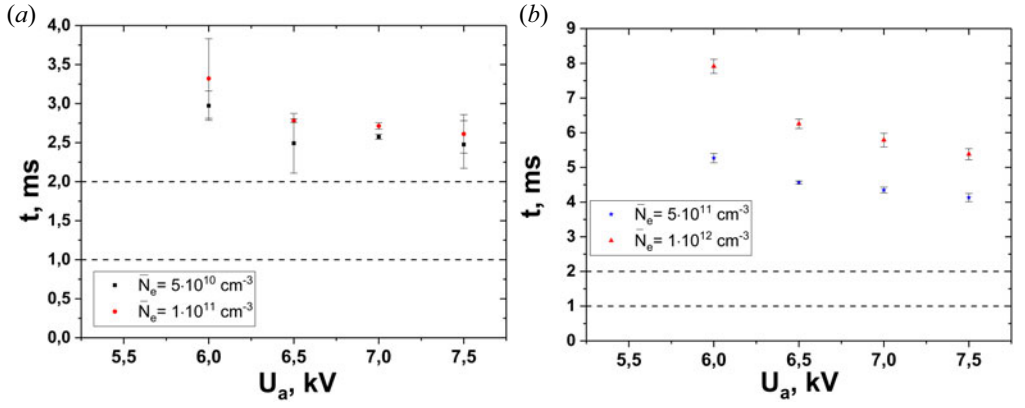


FIGURE 10. Time intervals to reach average plasma density (*a*) 5×10^{10} and 1×10^{11} cm^{-3} and (*b*) 5×10^{11} and 1×10^{12} cm^{-3} as a function of the anode voltage on the generator K-1. Dashed lines show time moments of K-1 anode voltage increase.

He II 468.6 nm are 26.3 and 51.0 eV, accordingly (Kramida *et al.* 2019). The oxygen atoms and ions appear in the discharge from electron impact excitation of O_2 and other oxide molecules (e.g. water) during dissociative electron impact processes (Itikawa 2001).

Some time after all the registered lines started to emit, the interferometer signal appears. Figure 10 shows the dependences of time interval needed for the average density to reach a certain value on the RF generator anode voltage. The dependences are ramp-down. They are weaker for low-density values and stronger for high-density values. This is an indirect indication that the electron temperature decreases with the plasma density increase.

As can be seen from the data obtained, the production time of the average plasma density of 1×10^{12} cm^{-3} is less than 10 ms.

The times of appearance the optical line emissions and the times of reaching certain plasma density levels have a tendency to decrease with the anode voltage increase that is typical for the above shots. One can suggest that the electron temperature is higher for the higher anode voltage at the same other conditions. Thus, the inelastic collision rates increase with the electron temperature that happens when the trend of the corresponding

https://doi.org/10.1017/S0022377820001099 Published online by Cambridge University Press

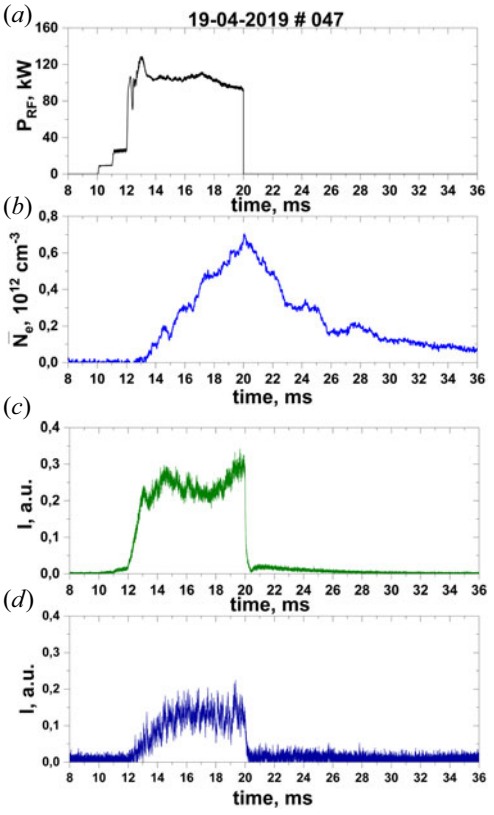


FIGURE 11. Time evolutions of (*a*) RF power and (*b*) average plasma density, and optical emission intensities of (*c*) H_Δ, 410.1 nm and (*d*) O II, 441.5 nm. The K-1 anode voltage is $U_a = 6$ kV.

rate coefficients is positive. This occurs when the electron energy is not so high, below 200 eV, the energy for the maximum electron impact ionization cross-section for helium (see Sorokin *et al.* 2004).

3.3. *Chord measurements*

The chord measurements in a shot-by-shot regime for the optical lines He I and He II was carried out at the He pressure $p = 0.145$ Pa; magnetic field at the device axis $B_0 = 0.347$ T, $K_\varphi = 0.318$, poloidal correctional coil current $I_{corr} = 447$ A and K-1 generator frequency $f = 5.13$ MHz. The K-1 generator operated as follows: start at 10 ms, the first power increase at 11 ms (step 1), the second power increase at 12 ms (step 2) and switch-off at 20 ms; the anode voltage was $U_a = 5$ kV. The time dependences of RF power, average density and H_Δ and O II spectral line intensities for these conditions are shown in figure 11.

For this experimental series, the location of the chords with reference to the impact parameter is shown in figure 6. The measurement results for the optical lines He I and He II are presented in figure 12. Drawings are of a similar shape despite the fact that in the first case, light is emitted by neutral helium atoms, and in the second case, by ions. As can be seen in figure 12(*a*,*b*), the radiation sources have the same dimensions as the plasma column ($|P| < 18$ cm), with the ion luminescence region being somewhat smaller than that in the case of atoms. It can also be seen that the emission of the He I and He II lines

https://doi.org/10.1017/S0022377820001099 Published online by Cambridge University Press

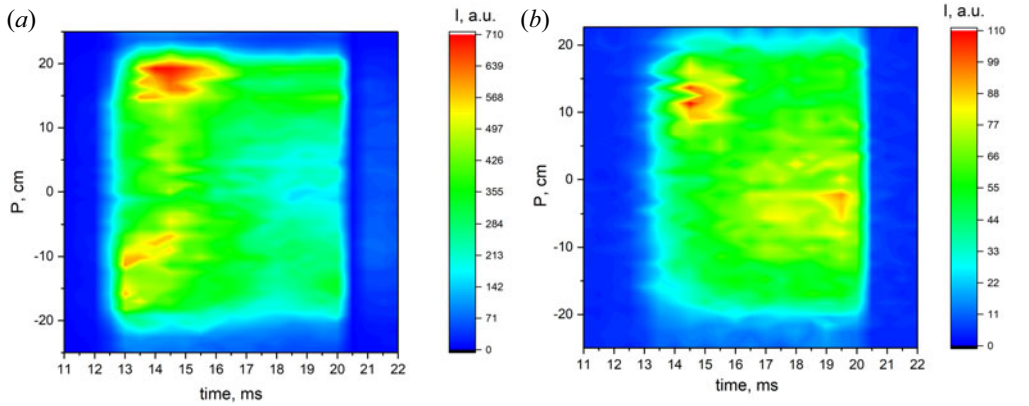


FIGURE 12. Time evolution of (*a*) He I and (*b*) He II chord distribution. He I wavelength is 447.15 nm, He II wavelength is 468.6 nm and P is the impact parameter (see figure 5).

along the chords changes in time, and the dependence of the line intensities on the impact parameter is not symmetric. Note that the average plasma density also changes in time (see figure 11*b*). Because the plasma production is transient and could be accompanied by plasma non-uniformity along the flux surface, conclusions on the profile shapes are hard to draw in this particular case.

3.4. *Discussion of wave propagation*

In the studied scenario, the presence of the hydrogen ion cyclotron zone is necessary. Otherwise, the density of plasma produced is lower by orders of magnitude. This allows one to suggest a significant role of hydrogen ions in the plasma production process. Plasma production can occur with ion impact ionization (Moiseenko 1980). High ion energy is needed in such a case to effectively ionize the neutral gas; the helium ions ionization cross-section is 10^{-17} cm^2 for 10 keV protons (Janev *et al.* 1987). In addition, indirect plasma production mechanism is possible when the hot ions heat the electrons via Coulomb collisions and, then, the electrons ionize the neutral gas. This mechanism is similar to that taking place at plasma production with the NBI. Such a mechanism provides slow plasma production, and the bottleneck is a low ion–electron collision rate (Kaneko *et al.* 2002; GRADIC *et al.* 2015). In our experiments, the plasma generation delay is small. This means that the electrons obtain energy directly from the RF field.

The RF heating of electrons is connected to the wave processes in the plasma. The helium majority ions generally determine the plasma dielectric response on the RF field. The ion cyclotron frequency for both singly and doubly ionized helium is lower than the RF frequency. The fast magnetosonic wave (FMSW) is propagating in such conditions. It is absorbed poorly by the cold plasma electrons but can be absorbed in the cyclotron resonance zone for the minority hydrogen ions.

The two-strap poloidal antenna can excite the slow wave (SW) less compared with FMSW. However, SW can play an important role in the plasma production process. Its dispersion equation reads

$$k_\perp^2 = -\frac{\varepsilon_\parallel}{\varepsilon_\perp}(k_\parallel^2 - k_0^2\varepsilon_\perp). \tag{3.1}$$

Here $k_\parallel = \boldsymbol{k}\cdot\boldsymbol{B}/B$, $k_\perp^2 = k^2 - k_\parallel^2$, $\varepsilon_\parallel = \boldsymbol{B}\cdot\hat{\boldsymbol{\varepsilon}}\cdot\boldsymbol{B}/B^2$, $\varepsilon_\perp = (\boldsymbol{r}\times\boldsymbol{B})\cdot\hat{\boldsymbol{\varepsilon}}\cdot(\boldsymbol{r}\times\boldsymbol{B})/|\boldsymbol{r}\times\boldsymbol{B}|^2$, where $\hat{\boldsymbol{\varepsilon}}$ is the plasma dielectric tensor, $\boldsymbol{r}$ is the radius vector and $\boldsymbol{B}$ is the

https://doi.org/10.1017/S0022377820001099 Published online by Cambridge University Press

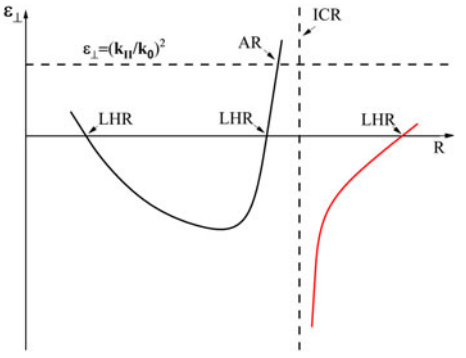


FIGURE 13. Sketch of $\varepsilon_\perp$ behaviour along the major radial chord.

magnetic field vector. The longitudinal tensor component is negative $\varepsilon_\parallel < 0$ in a cold plasma, and SW can propagate in plasma ($k_\perp^2 > 0$) where $\varepsilon_\perp > 0$. The SW can be damped owing to the imaginary part of $\varepsilon_\parallel$ and in this case delivers its energy to the plasma electrons (Lyssoivan *et al.* 1992). The imaginary part appears owing to the electron binary collisions, mainly with the neutral gas. A contribution to the imaginary part is also made by the Landau damping on electrons, especially at low RF generator frequencies.

Figure 13 shows the $\varepsilon_\perp$ behaviour along the major radial chord. There are three zones of SW propagation: two are at the plasma edge and one in the centre of the plasma column. All three zones are ended with zero-valued $\varepsilon_\perp$. When $\varepsilon_\perp \to \pm 0$, following (3.1), $k_\perp^2 \to \pm\infty$, and this is the lower hybrid resonance point. The SW travels in a direction opposite to the $\varepsilon_\perp$ gradient and reaches a lower hybrid resonance point where it is fully damped without reflections (Fidone & Granata 1971; Moiseenko, Wauters & Lyssoivan 2016). At two SW propagation zones at the plasma edge, the plasma properties are determined by the majority ions, helium, and the plasma density corresponding to the lower hybrid resonance can be estimated as $N_e \approx 3 \times 10^9$ cm^{-3} for 5.1 MHz generator frequency. This suggests that the SW propagation zone near the antenna provides plasma production at the early stage of the RF discharge (Lyssoivan *et al.* 2014).

The two-strap antenna excites waves with a broad $k_\parallel$ spectrum. It $k_\parallel$ is large enough, $k_\parallel > \omega/v_{th,e}$ (where $v_{th,e}$ is the thermal electron speed), then $\varepsilon_\parallel$ changes its sign from negative to positive. The wave propagates inside the plasma column in such a case in the region where $\varepsilon_\perp < 0$, and is absorbed by plasma electrons through the Landau mechanism. The zone between the antenna and the lower hybrid resonance point then becomes the zone of cut-off, and the wave tunnelling comes into play. As plasma density increases, the lower hybrid resonance point shifts closer to the antenna, and the tunnelling becomes better together with the antenna–wave coupling.

A more powerful plasma heating mechanism appears when there is a hydrogen cyclotron resonance zone inside the plasma column. The minority contribution to $\varepsilon_\perp$, $\varepsilon_{\perp\mathrm{H}}$, has a singularity at the point of ICR that is cancelled by the collision frequency or the Doppler shift. At a higher magnetic field than the resonant one, $\varepsilon_{\perp\mathrm{H}} > 0$ and its value can exceed the negative contribution of the majority ions. There, the SW propagation zone appears. It is bounded by the lower hybrid resonance from the left (see figure 13) and a cut-off point from the right, which obeys the condition $\varepsilon_\perp = (k_{||}/k_0)^2$ that can be obtained from (3.1). The cut-off point for SW is the conversion point [Alfvén resonance (AR)] of FMSW to SW. The generated by the FMSW field SW propagates inside the torus according to (2.1),

https://doi.org/10.1017/S0022377820001099 Published online by Cambridge University Press

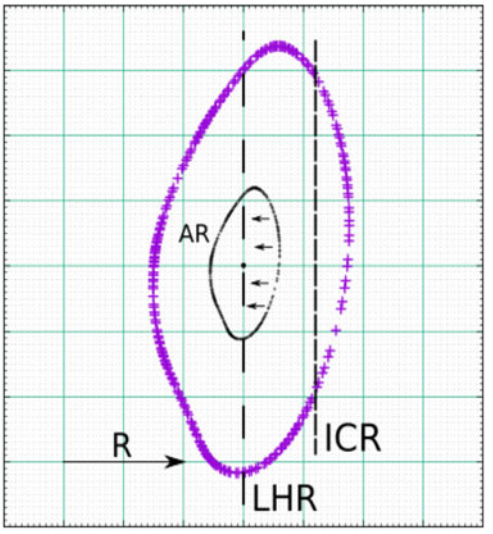


FIGURE 14. Sketch illustrating FMSW conversion into SW in the presence of a minority inside the plasma column.

reaches the point of low hybrid resonance (LHR) where it is totally absorbed (Klima, Longinov & Stepanov 1975).

In two- and three-dimensional non-uniform plasma, the electron heating pattern is more complicated. Following the papers by Hellsten & Tennfors (1984) and Moiseenko & Tennfors (1996), in the limit of infinite conductivity of plasma along the magnetic field lines, the conversion occurs near the magnetic surface. The case of finite conductivity was treated numerically in two dimensions for tokamaks (see, e.g., Lin *et al.* 2003). Even in the qualitative sense, the results are doubtfully applicable to our case because the calculations were done for hot fully ionized plasma with a temperature about two orders of magnitude higher than in our experiment.

For efficient conversion, it is necessary that this magnetic surface does not intersect the cyclotron zone. Such a heating scheme needs to select a heating frequency lower than ion cyclotron one at the device axis (see figure 14). This is confirmed in our experiment.

It is necessary to note that previously described scenario was developed initially for plasma heating and successfully used for this (see, e.g., Majeski *et al.* 1996). Thus, after plasma production, with higher RF power the scenario could continue for plasma heating.

4. Summary and conclusion

In support of the ICRF experiments planned on the W7-X stellarator, that is, fast ion generation, wall conditioning, target plasma production and heating, a first experimental study on plasma production has been made in the U-2M stellarator using a W7-X-like two-strap antenna.

The first experimental results of ICRF discharges created with the W7-X-like antenna in certain regimes have been presented in this paper. For all the experiments, antenna phasing is a monopole. The W7-X-like antenna experiments with launched RF power of $\sim$100 kW have been performed in helium ($p = (4\text{–}14) \times 10^{-2}$ Pa) with the vessel walls pre-loaded with hydrogen. Production of plasma with a density higher than 10^{11} cm^{-3} has been observed near the fundamental harmonic of the hydrogen cyclotron frequency. Operation at first hydrogen harmonic is feasible in W7-X future ICRF experiments.

https://doi.org/10.1017/S0022377820001099 Published online by Cambridge University Press

In experiments at U-2M, an ICRF plasma with an average density of $\sim(2–2.6) \times 10^{12}$ cm^{-3} has been produced.

The discharges of such type have been described and the three stages of discharge development have been identified. The dependences of measured quantities on the discharge parameters have been analysed. The dependence of the final average plasma density on the generator anode voltage (the launched power) saturates at high voltage values. Analysis of the OES data reveals that after the RF power launch, the H_Δ line appears first, then the He I line after a small delay. The delay for He II and O II lines is quite long and becomes shorter with increasing RF power. The rate of plasma production is almost independent of the launched RF power at the initial plasma production stage and increases with power at further stages. The chord distribution of He I and He II lines luminosity are almost the same.

In the RF plasma production scenarios, RF generator operation without load is unavoidable. This happens at the initial stage of plasma production and could result in arcing. If the no-load stage is short, the probability of arcing is reduced to negligible values. In the scenario of plasma build-up studied, the no-load time is very small, 2–3 ms.

A short plasma production time indicates that at all stages of plasma production the electrons are intensively heated by the RF field. The SW may play a key role in this. At the initial stage of plasma production, the direct SW excitation by the antenna comes into play. At higher plasma densities, the mode conversion minority scenario of electron heating is realized.

The studied plasma production scenario looks promising and could possibly be used in machines larger than U-2M. The minority of hydrogen in the helium atmosphere is possible at W-7X, and the RF power at 26 MHz is available for a magnetic field of 1.7 T. The topologies of the magnetic field module at the antenna locations in U-2M and W7-X are not so different. In addition, the structure of the antenna currents is similar. If such a scenario could be realized at W7-X, higher RF power is necessary. One could suggest that power is proportional to the plasma volume. Under this assumption, the necessary ICRH power is 0.9–1.8 MW and such power will be available at W7-X.

The same can be said about the experiment on LHD (Komori *et al.* 2010). There, for the RF frequency of 38.5 MHz, a 2.6 T magnetic field is available.

Acknowledgements

This work has been carried out within the framework of the EUROfusion Consortium and has received funding from the Euratom research and training programme 2014–2018 and 2019–2020 under Grant Agreement No. 633053. The views and opinions expressed herein do not necessarily reflect those of the European Commission. This work also received funding from National Academy of Sciences of Ukraine (grants P-3-22 and TsV-5-20).

Editor Per Helander thanks the referees for their advice in evaluating this article.

Declaration of interests

The authors report no conflict of interest.

REFERENCES

Äkäslompolo, S., Drewelow, P., Gao, Y., Ali, A., Asunta, O., Bozhenkov, S., Fellinger, J., Ford, O. P., den Harder, N., Hartmann, D. *et al.* 2019 Validating fast-ion wall-load IR analysis-methods against W7-X NBI empty-torus experiment. *J. Instrum.* **14**, P07018.

https://doi.org/10.1017/S0022377820001099 Published online by Cambridge University Press

BELETSKII, A. A., BEREZHNYJ, V. L., BURCHENKO, P. YA., CHECHKIN, V. V., CHERNYSHENKO, V. YA., GRIGOR'EVA, L. I., GUBAREV, S. P., KONOVALOV, V. G., KULAGA, A. E., KURILO, D. V. *et al.* 2008 First results of the renewed URAGAN-2M torsatron. *Probl. At. Sci. Technol. Ser.: Plasma Phys*. **6**, 13–15.

BRAKEL, R., HARTMANN, D., GRIGULL, P. & W7-AS TEAM 2001 ICRF wall conditioning experiments in the W7-AS stellarator. *J. Nucl. Mater*. **290**, 1160–1164.

BYKOV, V. E., GEORGIEVSKIJ, A. V., DEMCHENKO, V. V., KUZNETSOV, YU. K., LITVINENKO, YU. A., LONGINOV, A. V., PAVLICHENKO, O. S., RUDAKOV, V. A., STEPANOV, K. N. & TOLOK, V. T. 1990 URAGAN-2M: a torsatron with an additional toroidal field. *Fusion Technol*. **17**, 140–147.

CARTER, M. D., LYSOJVAN, A. I., MOISEENKO, V. E., NAZAROV, N. I., SHVETS, O. M. & STEPANOV, K. N. 1990 Plasma production using radiofrequency fields near or below the ion cyclotron range of frequencies. *Nucl. Fusion* **30**, 723–730.

VAN EETEN, P., KALLMEYER, J. P., MCNEELY, P., RUST, N., HARTMANN, D., SCHACHT, J., NAUJOKS, D., DEGENKOLBE, S., VILBRANDT, R., BOSCHTHE, H. S. *et al.* 2019 W7-X NBI beam dump thermocouple measurements as safety interlock. *Fusion Engng Des*. **146**, 1329–1333.

ERCKMANN, V., BRAND, P., BRAUNE, H., DAMMERTZ, G., GANTENBEIN, G., KASPAREK, W., LAQUA, H. P., MAASSBERG, H., MARUSHCHENKO, N. B., MICHEL, G. *et al.* 2007 Electron cyclotron heating for W7-X: physics and technology. *Fusion Sci. Technol*. **52**, 291.

ESSER, H. G., LYSSOIVAN, A., FREISINGER, M., KOCH, R., VAN OOST, G., WESCHENFELDER, F., WINTER, J. & TEXTOR-ICRH-TEAM 1997 ICRF wall conditioning at TEXTOR-94 in the presence of a 2.25 T magnetic field. *J. Nucl. Mater*. **241**, 861–866.

FIDONE, I. & GRANATA, G. 1971 Propagation of electromagnetic waves in a plasma with a sheared magnetic field. *Nucl. Fusion* **11**, 133–139.

GAUTHIER, E., DE LA CAL, E., BEAUMONT, B., BECOULET, A., GIL, C., GRISOLIA, C., GROSMAN, A., HUTTER, T., KUUS, H. & LADURELLE, L. 1997 Wall conditioning technique development in Tore Supra with permanent magnetic field by ICRF wave injection. *J. Nucl. Mater*. **241**, 553–558.

GEIGER, J., BEIDLER, C. D., FENG, Y., MAAßBERG, H., MARUSHCHENKO, N. B. & TURKIN, Y. 2015 Physics in the magnetic configuration space of W7-X. *Plasma Phys. Control. Fusion* **57**, 014004.

GRADIC, D., DINKLAGE, A., BRAKEL, R., MCNEELY, P., OSAKABE, M., RUST, N., WOLF, R. & THE W7-X TEAM AND THE LHD EXPERIMENTAL GROUP 2015 Assessment of the plasma start-up in Wendelstein 7-X with neutral beam injection. *Nucl. Fusion* **55**, 033002.

HAYWARD, W. 1994 *Introduction to Radio Frquency Design*. ARRL. p. 138.

HELLSTEN, T. & TENNFORS, E. 1984 Resonance surfaces in the ion cyclotron frequency range in toroidal systems. *Phys. Scr*. **30**, 341–345.

HU, J. S., LI, J. G. & HT-7 TEAM 2007 Differences of ICR cleanings in He, D_2 and O_2 for deposit removal and hydrogen release in HT-7. *J. Nucl. Mater*. **366**, 206–215.

HU, J. S., LI, J. G., ZHAO, Y. P. & EAST TEAM 2008 He–ICR cleanings on full metallic walls in EAST full superconducting tokamak. *J. Nucl. Mater*. **376**, 207–210.

ITIKAWA, Y. (Ed.) 2001 *Elementary Particles, Nuclei and Atoms. Volume 17. Photon and Electron Interactions with Atoms, Molecules and Ions. Subvolume C. Interactions of Photons and Electrons with Molecules*. Springer-Verlag.

JANEV, R. K., LANGER, W. D., EVANS, K. JR. & POST, D. E. JR. 1987 *Elementary Processes in Hydrogen-Helium Plasmas. Cross Sections and Reaction Rate Coefficients*. Springer-Verlag.

KANEKO, O., TAKEIRI, Y., TSUMORI, K., OKA, Y., OSAKABE, M., IKEDA, K. & LHD EXPERIMENTAL GROUP 2002 Analysis of plasma initiation by neutral beams in the Large Helical Device. *Nucl. Fusion* **42**, 441–447.

KLIMA, R., LONGINOV, A. V. & STEPANOV, K. N. 1975 High-frequency heating of plasma with two ion species. *Nucl. Fusion* **15**, 1157–1171.

KLINGER, T., ANDREEVA, T., BOZHENKOV, S., BRANDT, C., BURHENN, R., BUTTENSCHÖN, B., FUCHERT, G., GEIGER, B., GRULKE, O., LAQUA, H. P. *et al.* 2019 Overview of first Wendelstein 7-X high-performance operation. *Nucl. Fusion* **59**, 112004.

https://doi.org/10.1017/S0022377820001099 Published online by Cambridge University Press

KOMORI, A., YAMADA, H., IMAGAWA, S., KANEKO, O., KAWAHATA, K., MUTOH, K., OHYABU, N., TAKEIRI, Y., IDA, K., MITO, T. *et al.* 2010 Goal and achievements of large helical device project. *Fusion Sci. Technol*. **58**, 1.

KOROVIN, V. B. & KRAMSKOY, E. D. 2012 Radio-frequency equipment for Uragan stellarators. *Probl. At. Sci. Technol. Ser.: Plasma Phys*. **6**, 19–21.

KOVTUN, Y. V., SHAPOVAL, A. N. & SIUSKO, Y. V. 2019 Observation of multiply charged states ions in a high-power pulsed reflex discharge. *Plasma Sources Sci. Technol*. **28**, 105009.

KRAMIDA, A., RALCHENKO, Y., READER, J. & NIST ASD TEAM. 2019 NIST Atomic Spectra Database (ver. 5.7.1).

LI, J., SHIMADA, M., ZHAO, Y., HU, J., GONG, X., YU, Y. W., ZHUO, G. Z. *et al.* 2011 Wall conditioning towards the utilization in ITER. *J. Nucl. Mat*. **415**, S35.

LIN, Y., WUKITCH, S. J., BONOLI, P. T., MARMAR, E., MOSSESSIAN, D., NELSON-MELBY, E., PHILLIPS, P., PORKOLAB, M., SCHILLING, G., WOLFE, S. *et al.* 2003 Ion cyclotron range of frequencies mode conversion electron heating in deuterium–hydrogen plasmas in the Alcator C-Mod tokamak. *Plasma Phys. Control. Fusion* **45**, 1013.

LOZIN, A. V., MOISEENKO, V. E., GRIGOR'EVA, L. I., KOZULYA, M. M., KRASYUK, A. YU., KULAGA, A. E., KRAMSKOY, E. D., LYSSOIVAN, A. I., MAZNICHENKO, S. M., MIRONOV, YU. K. *et al.* 2013 Usage of three-half-turn antenna at the URAGAN-3M device. *Probl. At. Sci. Technol. Ser.: Plasma Phys*. **83** (1), 27–29.

LYASHCHENKO, V. N., OZHEREL'EV, F. I., REVA, S. N., TSIBLIEV, D. A. 2009 Synchronization system for experiments research installation Uragan-2M. *J. Kharkiv Natl Univ. Phys. Ser. "Nuclei, Particles, Fields"* **880**, 113–119.

LYSSOIVAN, A., HARTMANN, D. A., NOTERDAEME, J. M., KOCH, R., BOBKOV, V., BLACKMAN, T., BRAUN, F., COX, M., DE VRIES, P., ESSER, H. G. *et al.* 2005 Development of ICRF wall conditioning technique on divertor-type tokamaks ASDEX Upgrade and JET. *J. Nucl. Mater*. **337**, 456–460.

LYSSOIVAN, A., DOUAI, D., KOCH, R., ONGENA, J., PHILIPPS, V., SCHÜLLER, F. C., VAN EESTER, D., WAUTERS, T., BLACKMAN, T., BOBKOV, V. *et al.* 2012 Simulation of ITER full-field ICWC scenario in JET: RF physics aspects. *Plasma Phys. Control. Fusion* **54**, 074014.

LYSSOIVAN, A., WAUTERS, T., TRIPSÝ, M., BOBKOV, V., CROMBÉ, K., DOUAI, D., KRETER, A., NICOLAI, D., NOTERDAEME, J.-M., ROHDE, V. *et al.* 2014 Wave aspect of neutral gas breakdown with ICRF antenna in ICWC operation mode. In *41st EPS Conference on Plasma Physics*, vol. 38. P2.030.

LYSSOIVAN, A. I., MOISEENKO, V. E., SHVETS, O. M. & STEPANOV, K. N. 1992 Analysis of ICRF ($\omega < \omega_{ci}$) plasma production in large scale tokamaks. *Nucl. Fusion* **32**, 1361–1372.

MAJESKI, R., ROGERS, J. H., BATHA, S. H., BUDNY, R., FREDRICKSON, E., GREK, B., HILL, K., HOSEA, J. C., LEBLANC, B., LEVINTON, F. *et al.* 1996 Mode conversion heating and current drive experiments in TFTR. *Phys. Rev. Lett*. **76**, 764.

MARUSHCHENKO, N. B., ALEYNIKOV, P., BEIDLER, C. D., DINKLAGE, A., GEIGER, J., HELANDER, P., LAQUA, H. P., MAASSBERG, H., TURKIN, Y. & W7-X TEAM 2019 Reduced field Scenario with X3 heating in W7-X. *EPJ Web Conf*. **203**, 01006.

MOISEENKO, V. E. 1980 RF breakdown of a neutral gas by means of ions. *Fiz. Plazmy* **6**, 1174–1178. (in Russian).

MOISEENKO, V. E., STADNIK, YU. S., SCHVETS, O. M., STEPANOV, K. N., VOLKOV, E. D. & TERESHIN, V. I. 2007 RF plasma production in Uragan-2M torsatron. *AIP Conf. Proc*. **933**, 115–118.

MOISEENKO, V. E., BEREZHNYJ, V. L., BONDARENKO, V. N., BURCHENKO, P. YA., CASTEJÓN, F., CHECHKIN, V. V., CHERNYSHENKO, V. YA., DREVAL, M. B., GARKUSHA, I. E., GLAZUNOV, G. P. *et al.* 2011 RF plasma production and heating below ion-cyclotron frequencies in Uragan torsatrons. *Nucl. Fusion* **51**, 083036.

MOISEENKO, V. E., STADNIK, YU. S., LYSOIVAN, A. I. & KOROVIN, V. B. 2013 Self-consistent modeling of radio-frequency plasma generation in stellarators. *Plasma Phys. Rep*. **39**, 873–881.

https://doi.org/10.1017/S0022377820001099 Published online by Cambridge University Press

MOISEENKO, V. E., LOZIN, O. V., SHAPOVAL, A. M., DREVAL, M. B., KULYK, Y. S., MIRONOV, Y. K., ROMANOV, V. S., PASHNEV, V. K., SOROKOVOY, E. L., PETRUSHENYA, A. A. *et al.* 2016 Progress in stellarator research at IPP-Kharkov. *Nukleonika* **61**, 91–97.

MOISEENKO, V. E., LOZIN, A. V., KOZULIA, M. M., MIRONOV, YU. K., ROMANOV, V. S., KONOVALOV, V. G. & SHAPOVAL, A. N. 2017*a* Alfven plasma heating in stellarator Uragan-2M. *Ukrainian J. Phys*. **62**, 311–311.

MOISEENKO, V. E., LYSSOIVAN, A., WAUTERS, T., TRIPSKÝ, M., LOZIN, A. V., PAVLICHENKO, R. O., KOZULYA, M. M., DREVAL, M. B., MIRONOV, YU. K., ROMANOV, V. S. *et al.* 2017*b* Radio-frequency plasma start-up at Uragan-3M stellarator. *Probl. At. Sci. Technol. Ser.: Plasma Phys*. **1**, 54–59.

MOISEENKO, V. E., LOZIN, A. V., KOZULIA, M. M., KOROVIN, V. B., BELETSKII, A. A., BARON, D. I., GRIGOR'EVA, L. I., CHECHKIN, V. V., MIRONOV, YU. K., ROMANOV, V. S. *et al.* 2019 Three half-turn antennas start-up. *Probl. At. Sci. Technol. Ser.: Plasma Phys*. **1**, 263–266.

MOISEENKO, V. E. & TENNFORS, E. 1996 Localized global ICRF eigenmodes and conversion zones in a two-ion species tokamak. *Plasma Phys. Control. Fusion* **38**, 2133–2142.

MOISEENKO, V. E., WAUTERS, T. & LYSSOIVAN, A. 2016 Lower hybrid resonance: field structure and numerical modelling. *Probl. At. Sci. Technol. Ser.: Plasma Phys*. **6**, 44–47.

NÜHRENBERG, C. 2016 Free-boundary ideal MHD stability of W7-X divertor. *Nucl. Fusion* **56**, 076010.

ONGENA, J., MESSIAEN, A., VAN EESTER, D., SCHWEER, B., DUMORTIER, P., DURODIE, F., KAZAKOV, YE. O., LOUCHE, F., VERVIER, M., KOCH, R. *et al.* 2014 Study and design of the ion cyclotron resonance heating system for the stellarator Wendelstein 7-X. *Phys. Plasmas* **21**, 061514.

PANKRATOV, I. M., BELETSKII, A. A., BEREZHNYJ, V. L., BURCHENKO, P. YA., CHECHKIN, V. V., GRIGOR'EVA, L. I., HARTMANN, D., KOCH, R., KONOVALOV, V. G., KULAGA, A. YE. *et al.* 2010 Behavior of RF discharge plasmas in the Uragan-3M and Uragan-2M torsatrons. *Contrib. Plasma Phys*. **50**, 520–528.

PAVLICHENKO, O. S. 1993 First results from the URAGAN-2M torsatron. *Plasma Phys. Control. Fusion* **35**, B223–B230.

PAVLICHENKO, R. O., ZAMANOV, N. V. & KULAGA, A. E. 2017 First measurements of line electron density in Uragan-2M plasmas via 140 GHz heterodyne interferometer. *Probl. At. Sci. Technol. Ser.: Plasma Phys*. **1**, 257–260.

PAVLICHENKO, R. O., ZAMANOV, N. V. & KULAGA, A. E. 2018 A high speed 140 GHz microwave interferometer for density fluctuation measurements in Uragan-2M stellarator. *Probl. At. Sci. Technol. Ser.: Plasma Phys*. **6**, 332–335.

PEDERSEN, T. S., KÖNIG, R., JAKUBOWSKI, M., KRYCHOWIAK, M., GRADIC, D., KILLER, C., NIEMANN, H., SZEPESI, T., WENZEL, U., ALI, A. *et al.* 2019 First divertor physics studies in Wendelstein 7-X. *Nucl. Fusion* **59**, 096014.

SOROKIN, A. A., BEIGMAN, I. L., BOBASHEV, S. V., RICHTER, M. & VAINSHTEIN, L. A. 2004 Total electron-impact ionization cross sections of Helium. *J. Phys. B: At. Mol. Opt. Phys*. **37**, 3215.

TRIPSKÝ, M., WAUTERS, T., LYSSOIVAN, A., BOBKOV, V., SCHNEIDER, P. A., STEPANOV, I., DOUAI, D., VAN EESTER, D., NOTERDAEME, J.-M., VAN SCHOOR, M. *et al.* 2017 A PIC-MCC code RFdinity1d for simulation of discharge initiation by ICRF antenna. *Nucl. Fusion* **57**, 126043.

VOITSENYA, V. S., SHAPOVAL, A. N., PAVLICHENKO, R. O., PANKRATOV, I. M., CHECHKIN, V. V., MOISEENKO, A. E., LOZIN, A. V., DREVAL, N. B., GRIGOR'EVA, L. I., KONOVALOV, V. G. *et al.* 2014 Progress in stellarator research in Kharkov IPP. *Phys. Scr*. **T161**, 014009.

WAUTERS, T., BRAKEL, R., BREZINSEK, S., DINKLAGE, A., GORIAEV, A., LAQUA, H. P., MARSEN, S., MOSEEV, D., STANGE, T., SCHLISIO, G. *et al.* 2018 Wall conditioning by ECRH discharges and He-GDC in the limiter phase of Wendelstein 7-X. *Nucl. Fusion* **58**, 066013.

WAUTERS, T., BORODIN, D., BRAKEL, R., BREZINSEK, S., BRUNNER, K. J., BUERMANS, J., CODA, S., DINKLAGE, A., DOUAI, D., FORD, O. *et al.* 2020 Wall conditioning in fusion devices with superconducting coils. *Plasma Phys. Control. Fusion* **62**, 034002.

https://doi.org/10.1017/S0022377820001099 Published online by Cambridge University Press

WOLF, R. C., BOZHENKOV, S., DINKLAGE, A., FUCHERT, G., KAZAKOV, Y. O., LAQUA, H. P., MARSEN, S., MARUSHCHENKO, N. B., STANGE, T., ZANINI, M. *et al.* 2019 Electron-cyclotron-resonance heating in Wendelstein 7-X: A versatile heating and current-drive method and a tool for in-depth physics studies. *Plasma Phys. Control. Fusion* **61**, 014037.

ZALESKIJ, Y. G., KURILKO, P. I., NAZAROV, N. I., PLYUSNIN, V. V. & SHVETS, O. M. 1989 Start-up of HF plasma discharge in the Uragan-3 torsatron. *Fiz. Plazmy* **15**, 1424–1429. (in Russian).

https://doi.org/10.1017/S0022377820001099 Published online by Cambridge University Press